LEGIBILITY NOTICE

A major purpose of the Technical Information Center is to provide the broadest dissemination possible of information contained in DOE's Research and Development Reports to business, industry, the academic community, and federal, state and local governments.

Although a small portion of this report is not reproducible, it is being made available to expedite the availability of information on the research discussed herein.

LA-UR--89-2898

DE89 016612

Los Alamos National Laboratory is operated by the University of California for the United States Department of Energy under contract W-7405-ENG-36

TITLE

LAGRANGIAN ANALYSIS OF MIV GAUGE EXPERIMENTS ON PBX 9502 USING THE MASS-DISPLACEMENT MOMENT FUNCTION

AUTHOR(S)

Charles A. Forest, Jerry Wackerle, Jerry J. Dick
Stephen A. Sheffield and Donald R. Pettit

SUBMITTED TO

Ninth Symposium (Int'l) on Detonation
August 28 - September 1, 1989
Portland, Oregon

DISCLAIMER

Los Alamos
Los Alamos National Laboratory
Los Alamos, New Mexico 87545

FORM NO. 836 R4
ST. NO. 2629 5/81

LAGRANGIAN ANALYSIS OF MIV GAUGE EXPERIMENTS ON PBX 9502 USING THE MASS-DISPLACEMENT MOMENT FUNCTION*

Charles A. Forest, Jerry Wackerle, Jerry J. Dick
Stephen A. Sheffield and Donald R. Pettit
Los Alamos National Laboratory
Los Alamos, NM 87545

Magnetic Impulse-Velocity (MIV) gauges were used to measure the impulse and particle-velocity fields at discrete Lagrangian positions in two samples of the TATB explosive PBX 9502. Each sample was shock driven by a 6.4 mm layer of reacting superfine TATB (ρ_o = 1.80 g/cm^3), which was itself shocked by a gas driven projectile. The gauge histories of particle velocity and impulse, and the derived displacement history were simultaneously fit to the partial derivatives of the mass-displacement moment function employing a single set of parameters. (The function also gives volume, energy, pressure and their time derivatives.) With an assumed mixture equation of state, the reaction extent and reaction rate were calculated. The two experiments were compared and rate correlations were examined.

*Work performed under the auspices of the U. S. Department of Energy.

INTRODUCTION

Lagrangian analysis[1-6] is the application of the conservation laws of mass and momentum to flow data obtained from gauges embedded in a material. The gauges are designed to disturb the flow as little as possible, and in the Lagrangian analysis are assumed to be massless and moving with the flow. The analysis uses the measured variables (such as particle velocity, stress, and impulse) and the conservation laws to form surfaces over the Lagrangian (h, τ) domain of the measured variables and of derived variables (such as volume, stress, and energy). Generally, the surfaces are not fluid-dynamic solutions because certain essential information (such as the equation of state, constitutive relation, or reaction rate) needed to construct the solution is unknown and is itself the object of the experiment. Rather, approximating surfaces are formed that fit the data in some optimum way and that have a subset of the physical properties of a solution. The analysis for reaction rate is completed by the assumption of a reactant product equation of state $P = P(V, e, w)$, and its time derivative $P_\tau = -(\rho c)^2 V_\tau + P_w w_\tau$, where w = mass fraction of undecomposed reactant, e = specific energy, and V = specific volume.

The data set may comprise data from several experiments or a single experiment with multiple gauges, such as the MIV assembly described here.

Magnetic impulse and velocity (MIV) gauge assemblies[6] are used to record a material's response to shock waves, and in particular, to record an explosive's reactive response to such stimuli. The record consists of simultaneous histories of the impulse (I) and particle velocity (u) at a number (typically five) of distinct Lagrangian distance (h) positions.

The impulse gauge is an integrating velocity gauge and

$$I(h, \tau) = \int_h^{h_s(\tau)} u(h', \tau)\rho_0 dh' \quad ,$$

and also then by momentum conservation,

$$I(h,\tau) = \int_{\tau_s(h)}^{\tau} \Big[P(h,\tau') - P_o\Big] d\tau' \quad .$$

where

$h_s(\tau)$ = position of the shock,
$\tau_s(h)$ = arrival time of the shock,

and

P = the pressure.

These data, along with shock-front data, form the basis for a Lagrangian analysis in which approximations to I, u and other flow and state variables are constructed.

Commonly the method for constructing the surface u and I is the Path-Line Method[3] in which a family of lines (roughly parallel to the shock line) are chosen so that each line cuts each of the gauge histories. Then a one-dimensional fit is made of u and I on each line using as data the values of u and I at the intersections of the path line with the history lines.

This paper, however, constructs the surface by using a mass-displacement moment function $\alpha(h,\tau)$ for which u and I are partial derivatives. The value of α is unimportant; the importance of α is that it induces the proper relationship between the variables Δx (displacement), I (impulse), η (compression), u (particle velocity), and P (pressure), and that all the data are fitted simultaneously with one parameter set.

EXPERIMENT

The explosive PBX 9502 (TATB 95%/Kel-F 5%) at density $\rho_o = 1.89$ g/cm^3 is quite insensitive and its prompt shock initiation is beyond the capabilities of our current gas gun. Thus each of the samples of PBX 9502 was boosted by a reacting, but not detonating, layer of superfine TATB of density $\rho_o = 1.80$ g/cm^3. The superfine TATB was shocked by the gas gun projectile as

shown in Figure 1. Of course, the magnitude and profile of the shock entering the PBX 9502 depends upon the projectile velocity and the superfine booster thickness. Accordingly, three preliminary experiments were done to find an appropriate booster thickness. The last of these, the 6.4-mm thick superfine TATB booster, was a composite double wedge in which the shock track of each wedge face recorded. The two MIV experiments were both made with a 6.4-mm superfine booster. The projectile velocities, however, were slightly different.

For the composite double wedge (Shot G684), the shock trajectories of both faces were simultaneously recorded by a single streak camera. The TATB booster was impact shocked by a 11-mm VISTAL impactor (ρ_0 = 3.959) mounted on a gas-gun projectile with velocity of 1.112 mm/μs. The shock trajectories were each fit by a nonparametric data smoother TFLS that allowed a discontinuous derivative (shock velocity) at the TATB-PBX 9502 interface. The shock velocities are shown in Figure 2. The shock velocity of one side is higher throughout than that of the other side, which may have resulted from wave tilt. A portion of the initial shock trajectory was lost from each.

Similarly, in the MIV gauge experiments (Shots G705 and G717), the TATB boosters were shocked by VISTAL-faced gas-gun projectiles of velocities 1.116 and 1.134 mm/μs. The MIV gauge assemblies were placed at an angle of 30 ° relative to the charge face in the two-inch diameter PBX 9502 charges. Nominally, the impulse and particle-velocity gauges are located 1, 2, 3, 4, and 5-mm deep into the PBX 9502 and are isolated from two-dimensional effects for the duration of the experimental record. The shock-trajectory data are the shock arrival times at the particle-velocity gauges and the shock velocities inferred from the Hugoniot ($U_s = 2.773 + 1.899\ u_p$) and the shock-jump particle velocities. The shock arrival time is taken at the midrise of the particle-velocity gauge. The shock particle velocity is the extrapolated value of the particle-velocity history at the shock arrival time. The shock velocity from a simultaneous least squares fit of shock position and velocity are shown in Figure 2.

ANALYSIS

The method is centered on a simultaneous constrained least-squares fit to the function, partial deriva-

tives, and shock-path derivatives of the mass-displacement moment function,[7]

$$\alpha(h,\tau) = \int_{\tau_s(h)}^{\tau} d\tau' \int_{h}^{h_s(\tau')} u(h',\tau')\rho_o dh' \quad .$$

Note that

$$\alpha(h,\tau) = \int_{\tau_s(h)}^{\tau} I(h,\tau')d\tau' \quad ,$$

the impulse time integral, and that by reversing the order of integration

$$\alpha(h,\tau) = \int_{h}^{h_s(\tau)} \Big[X(h',\tau) - X_s(h')\Big]\rho_o dh' \quad .$$

the displacement moment, where $X(h,\tau)$ is the Euclidean space position and $X_s(h)$ is the Euclidean space position at shock arrival. Partial derivatives of α are the functions associated with mass and momentum conservation; only energy need be integrated separately. Figure 3 shows the partial derivatives of α; moving in the table diagonally downward left indicates differentiation in Lagrangian distance h and diagonally right indicates differentiation in time τ. For example then $\partial^2\alpha/\partial h^2 = \rho_o\eta$, $\partial^2\alpha/\partial\tau^2 = P - P_o$, and $\partial^2\alpha/\partial h\partial\tau = -\rho_o u$, where $\eta = 1 - V/V_o$ is the volume strain. On the shock line $\alpha(h, \tau_s(h)) = 0$, $\partial\alpha/\partial\tau = I = 0$, and $\partial\alpha/\partial h = -\rho_o\Delta X = 0$, where $\Delta X = X - X_s$. Furthermore, first derivatives of I and $-\rho_o\Delta X$ along the shock path yield the Rankine-Hugoniot shock-jump relations, and second derivatives are the kinematic shock-change equations. In practice α is represented as a function of time after shock arrival, thus $\alpha(h,\tau) = \beta(h, \tau - \tau_s(h))$ and properties of α are applied to β. Note that derivatives of α and β satisfy

$$\alpha_h = \beta_1 - \tau_s'\beta_2, \quad \alpha_\tau = \beta_2 \quad .$$

$$\alpha_{hh} = \beta_{11} - 2\tau_s'\beta_{12} + (\tau_s')^2\beta_{22} - \tau_s''\beta_2$$

$$\alpha_{\tau\tau} = \beta_{22} \text{ and}$$

$$\alpha_{\tau h} = \beta_{21} - \tau_s'\beta_{22} \quad .$$

Subscripts of 1 and 2 denote partial differentiation of $\mathcal{J}$ with respect to first and second arguments. The shock line is thus placed on the abscissa axis of the function $\mathcal{J}$. Thus $\mathcal{J}_{22}(h,0)$ is the pressure on the shock line and the shock-line conditions applied to $\mathcal{J}$ give $\mathcal{J}(h,0) = 0$ and $(\partial\mathcal{J}/\partial\tau)(h,0) = 0$, which reduces the number of parameters necessary for the least-square fit. The function may be expanded piecewise with each sub area being bounded by a time line similar to $\tau_s(h)$ and with appropriate continuity conditions applied.

For the least-squares fit of α, particle velocity and impulse data are entered as the partial derivatives $\alpha_{h\tau} = -\rho_o u$ and $\alpha_\tau = I$. Particle-velocity histories are also individually smoothed and integrated to give displacement data $\alpha_h = -\rho_o \Delta X$. The shock-trajectory pressure is determined by an independent least-squares fit (as described above) and is used as a constraint. The function $\mathcal{J}_{22}(h,0)$ is the shock pressure and is completely determined by the shock trajectory. Smoothing terms of $(\eta_{hh})^2, (u_{\tau\tau})^2$, and $(P_{\tau\tau})^2$ are added to the least-squares merit function. The smoothing is necessary to dampen the untoward effects on the volume strain η and other subsequently derived variables of energy, reaction extent and reaction rate caused by the gauge to gauge calibration uncertainty in particle velocity and impulse.

The streak-camera trace and the individual MIV gauge histories were fit by a new nonparametric least-square method Tabular Function Least Squares (TFLS). In this method the least-square function is represented as a table $\{z_i, f_i\}$, $i = 1, NF$ with an associated interpolation function G, where $G(\{z, f\}, x)$ = interpolated value at x. The table $\{z\}$ is uniformly spaced over the domain of the fit. (The current choices for G are linear or cubic interpolation on a central interval.) Smoothness is induced upon the table by adding to the merit function the sum of the squares of the Nth order forward-difference operator over the interior tabular points. Thus given data $\{(x_i, y_i)\}$, the merit function

$$E(\{f\}) = \sum_{i=1}^{ND} \left[G(\{z, f\}, x_i) - y_i \right]^2 + \mathrm{wt} \cdot \sum_{i=1}^{NF-N} (\Delta^N f_i)^2$$

is minimized with respect to the table $\{f_i\}$, where ND = number of data points, NF = number of tabular points, and N = order of the difference operator.

Following the determination of the function $\alpha(h, \tau)$ by least squares fitting, the reactant mass fraction w is found by solution of $P = P(V, e, w)$, an assumed solid and product mixture equation of state. The reactant (solid) EOS was taken to be a Mie-Grüneisen form with a first shock Hugoniot reference line. The parameters are $U_s = 2.773 + 1.809 u_p, \Gamma_0 = 1.50, \rho_0 = 1.893$. The product EOS was also a Mie-Grüneissen form with a BKW calculated detonation isentrope reference line.[8] Two mixture rules were applied. The first is temperature and pressure equilibrium. The second is pressure equilibrium with an isentropic solid in which solid isentrope for each mass point passes through its first shock (V, e, P) point.

RESULTS

Comparisons of the data, α surface lines, and derived reaction graphs for shots G705 and G717 are shown in Figures 4 through 13 with shot G705 appearing on the left. In Figure 4 and 5, the impulse and particle-velocity data histories and α partial-derivative lines are shown. The particle-velocity graphs show that shot G717 was subject to higher initial shock pressure. The impulse histories are similar but those of G717 are steeper, which is reflected in the pressure graphs of Figure 6. Constant-time profiles (snapshots) are shown in Figures 7, 8, and 9 at times of 0.2, 0.4, 0.6, 0.8, 1.0, and 1.2 μs. The snapshots verify that the α surface is well behaved between the gauge positions.

With the mixture equation of state, the mass fraction of reactant histories are calculated for Langrangian positions of 2.0, 2.5, 3.0, 3.5, and 4.0 mm; points well interior to the Lagrangian domain. Figure 10 shows the mass-fraction histories; no exponential first order reaction tail is seen, although such a feature may be lost in the least-squares fitting.

The time derivative of $-ln(w)$ is graphed versus pressure in Figure 11, which shows that the reaction rate is not a simple function of pressure. The reaction rate is graphed versus equilibrium temperature in Figure 12 and versus isentropic solid temperature in Figure 13. The isentropic solid temperature is dependent only on the initial shock and the subsequent solid compression history and therefore cannot be expected to closely reflect reaction. The solved reaction histories for the two equation of state mixture rules were indistinguishable.

Each of the reaction or reaction-rate graphs does show that the reaction rate is initially slow following the shock and increases in time thereafter, indicating some induction process.

Unfortunately, the reaction-rate function or system is not obvious from the common graphs and will require further study of rate forms for its deduction. A possible method to examine a reaction-rate function (or system) is to integrate the rate form by using the derived state histories and compare the integrated reactant histories to the derived reactant histories in the context of a nonlinear least-squares optimization.

REFERENCES

1. Fowles, R. and Williams, R. F., "Plane Stress Wave Propagation in Solids," J. App. Phys., Vol. 41, Jan. 1970, p. 360

2. Cowperthwaite, M. and Williams, R. F., "Determination of Constitutive Relationships with Multiple Gauges in Nondivergent Waves," J. App. Phys., Vol. V2, No. 1, Jan. 1971, p. 456.

3. Grady, D. E., "Experimental Analysis of Spherical Wave Propagation," J. of Geophysical Research, Vol. 78, No. 8, March 10, 1973, p. 1299.

4. Seamon, L., "Lagrangian Analysis for Multiple Stress or Velocity Gauges in Attenuating Waves," J. Appl. Phys., Vol 45, No. 10, Oct. 1974, p. 4303.

5. Vantine, H. C., Rainberger, R. B., Curtis, W. D., Lee, R. S., Cowperthwaite, M., and Rosenberg, J. T., "The Accuracy of Reaction Rates Inferred from Lagrangian Analysis and In-Situ Gauge Measurements," Proceedings Seventh Symposium (Int'l) on Detonation, NSWC MP 82-334, Annapolis, Maryland, June 1981, p. 466.

6. Vorthman, J., Andrews, G., and Wackerle, J., "Reaction Rates From Electromagnetic Gauge Data," Proceedings Eighth Symposium (Int'l) on Detonation, NSWC MP 86-194, Albuquerque, New Mexico, July 1985, p. 99.

7. Forest, C. A., "Impulse Time-Integral Function and Lagrangian Analysis," Proceeding of the American Physical Society 1989 Topical Conference on Shock Compression of Condensed Matter, (Eds. Schmidt, S. C., Johnson, J. N., and Davison, L. W.), Albuquerque, New Mexico, August 1989.

8. Mader, C. L., Numerical Modeling of Detonations, University of California Press, Berkeley, 1979, p. 412.

FIGURE 1. MIV GAUGE EXPERIMENTAL ASSEMBLY.

FIGURE 2. SHOCK TRAJECTORY VELOCITIES FOR DOUBLE WEDGE SHOT G684 (LINES), MIV SHOT G705 (CIRCLES). AND MIV SHOT G717 (SQUARES).

FIGURE 3. THE FUNCTION α AND ITS PARTIAL DERIVATIVES.

FIGURE 4. IMPULSE GAUGE DATA AND α_τ LINES FOR SHOTS G705 (LEFT) AND G717 (RIGHT).

FIGURE 5. PARTICLE VELOCITY GAUGE DATA AND $-V_0\alpha_{h,\tau}$ LINES FOR SHOTS G705 (LEFT) AND G717 (RIGHT).

FIGURE 6. PRESSURE AT THE GAUGES ($\alpha_{\tau\tau}$) FOR SHOTS G705 (LEFT) AND G717 (RIGHT).

FIGURE 7. PARTICLE VELOCITY SNAPSHOT PROFILES AT SIX TIMES ($t = 0.2, 0.4, \cdots, 1.2$) FOR SHOTS G705 (LEFT) AND G717 (RIGHT).

FIGURE 8. DENSITY SNAPSHOT PROFILES AT SIX TIMES ($t = 0.2, 0.4, \cdots, 1.2$) FOR SHOTS G705 (LEFT) AND G717 (RIGHT).

FIGURE 9. PRESSURE SNAPSHOT PROFILES A SIX TIMES ($t = 0.2, 0.4, \cdots, 1.2$) FOR SHOTS 705 (LEFT) AND G717 (RIGHT).

FIGURE 10. MASS FRACTION OF REACTANT HISTORIES AT h = 2.0, 2.5, 3.0, 3.5, and 4.0 FOR SHOTS G705 (LEFT) AND G717 (RIGHT).

FIGURE 11. TIME DERIVATIVE OF $-ln(w)$ HISTORIES AT h= 2.0, 2.5, 3.0, 3.5 and 4.0 FOR SHOTS G705 (LEFT) AND G717 (RIGHT).

FIGURE 12 REACTION RATE HISTORIES VERSUS EQUILIBRIUM TEMPERATURE AT h= 2.0 2.5, 3.0, 3.5 and 4.0 FOR SHOTS G705 (LEFT) AND G717 (RIGHT).

FIGURE 13. REACTION RATE HISTORIES VERSUS ISENTROPIC SOLID TEMPERATURE AT h = 2.0, 2.5, 3.0, 3.5 and 4.0 FOR SHOTS G705 (LEFT) AND G717 (RIGHT).

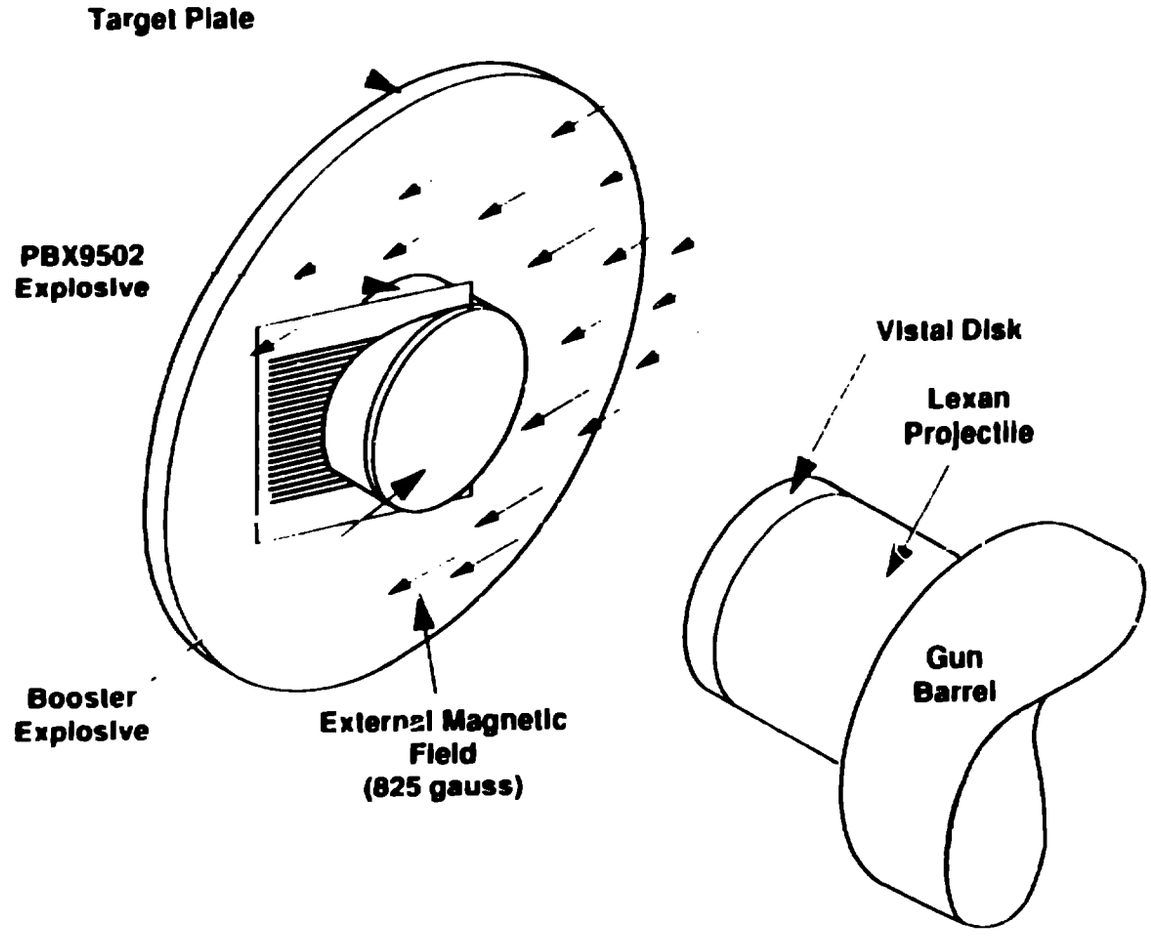

FIGURE 1. MIV GAUGE EXPERIMENTAL ASSEMBLY.

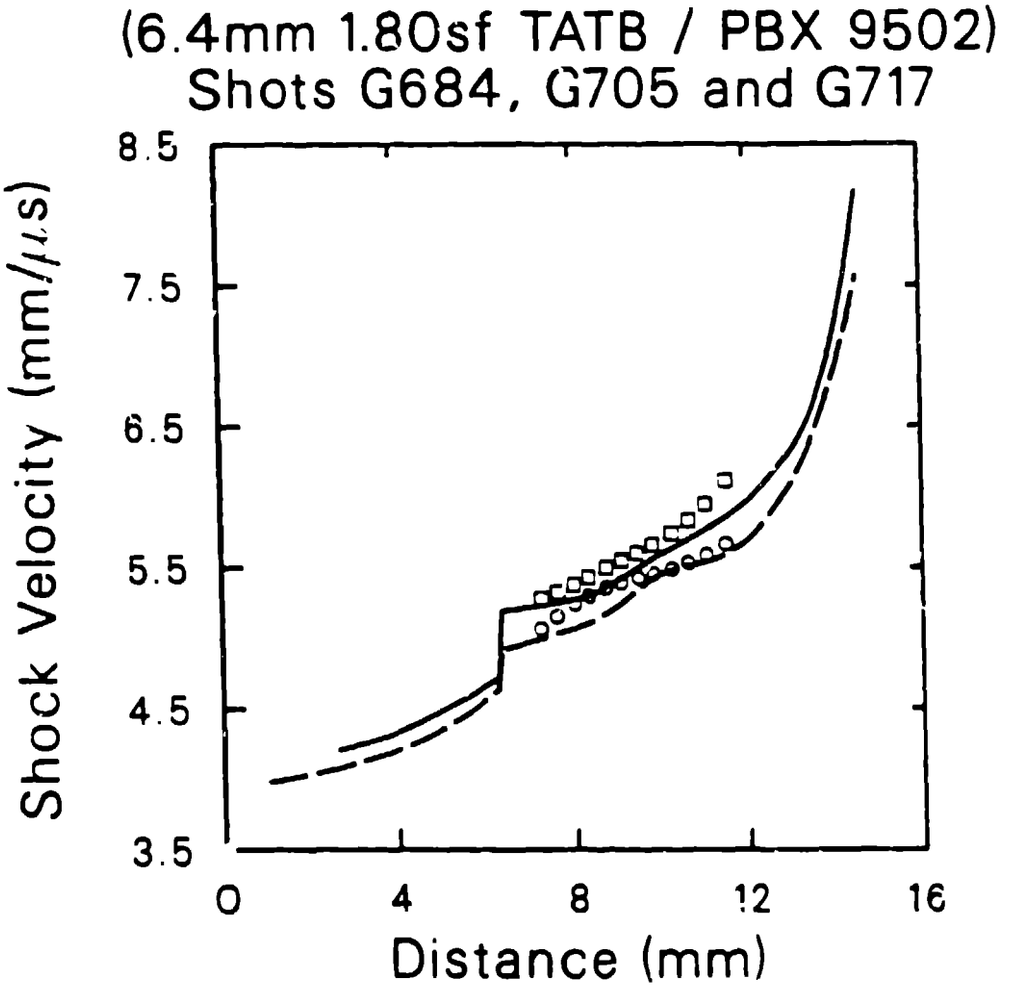

FIGURE 2. SHOCK TRAJECTORY VELOCITIES FOR DOUBLE WEDGE SHOT G684 (LINES), MIV SHOT G705 (CIRCLES), AND MIV SHOT G717 (SQUARES).

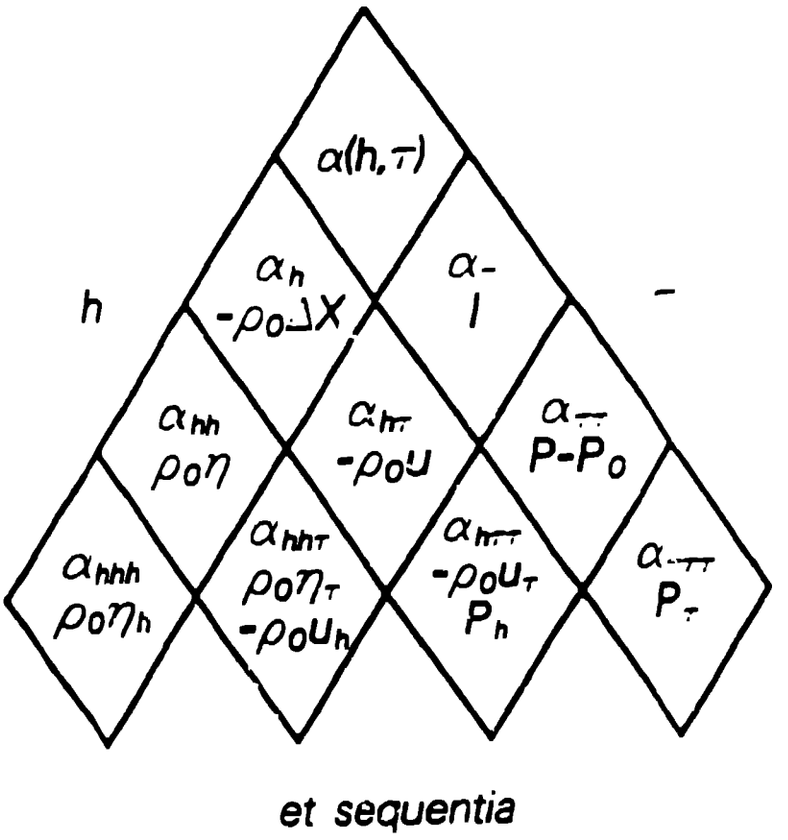

FIGURE 3. THE FUNCTION α AND ITS PARTIAL DERIVATIVES.

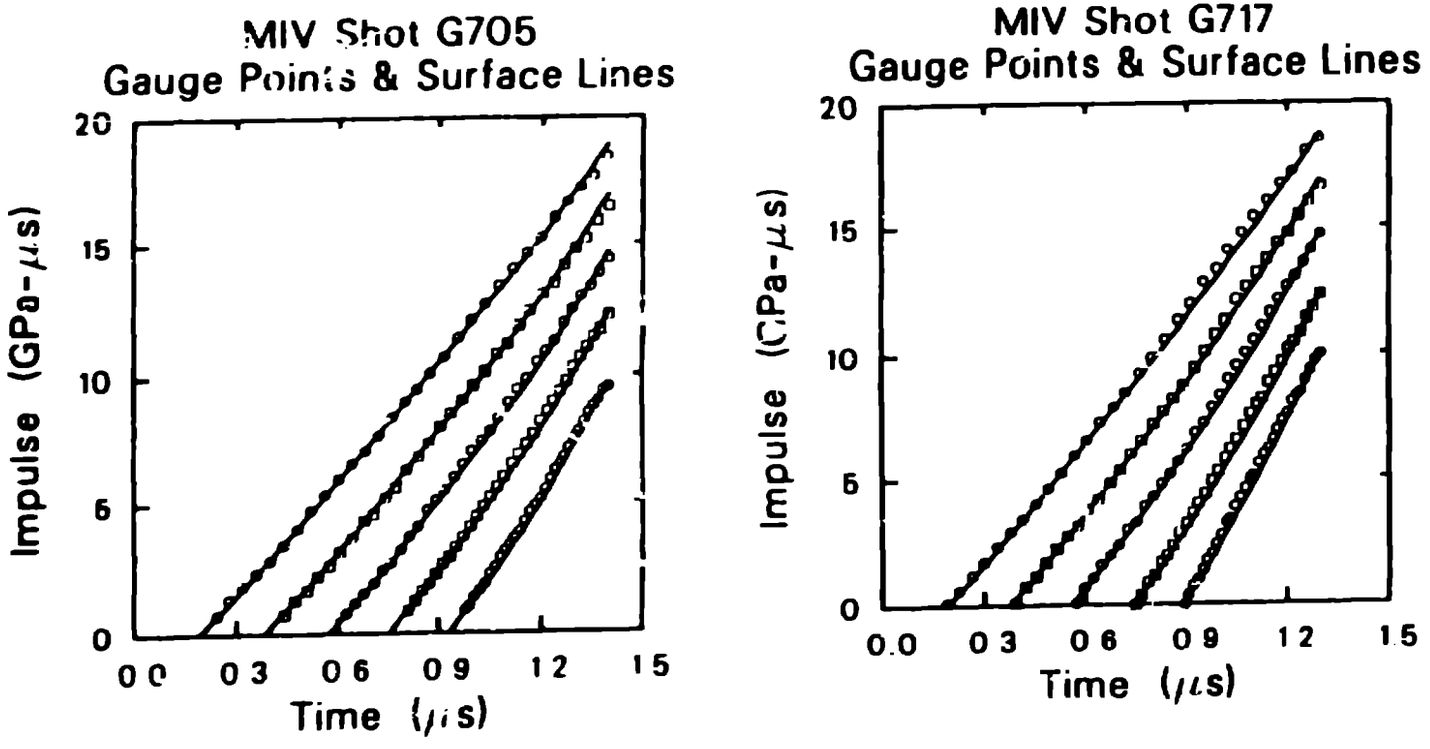

FIGURE 4. IMPULSE GAUGE DATA AND σ_y FIT LINES FOR SHOTS G705 (LEFT) AND G717 (RIGHT).

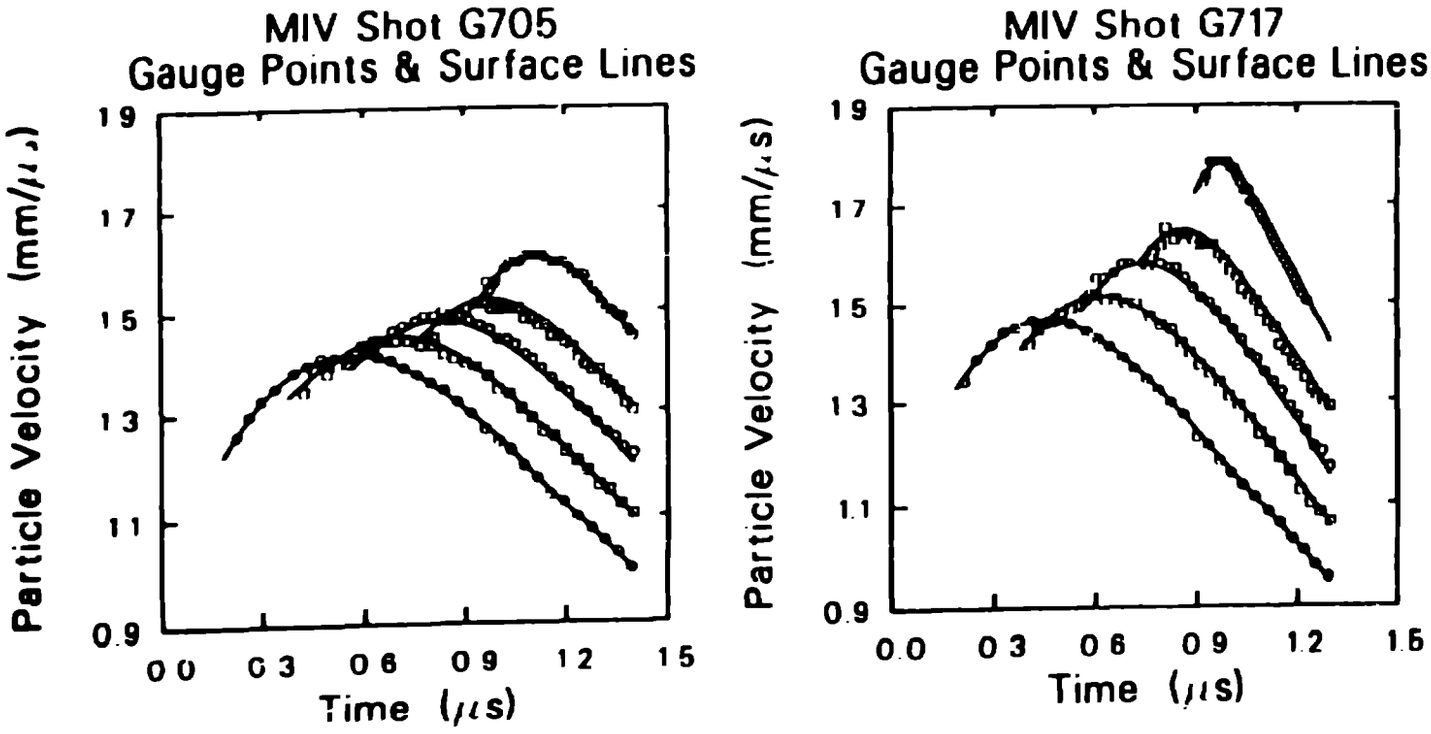

FIGURE 5. PARTICLE VELOCITY GAUGE DATA AND $-V_{0}\sigma_{h,r}$ LINES FOR SHOTS G705 (LEFT) AND G717 (RIGHT).

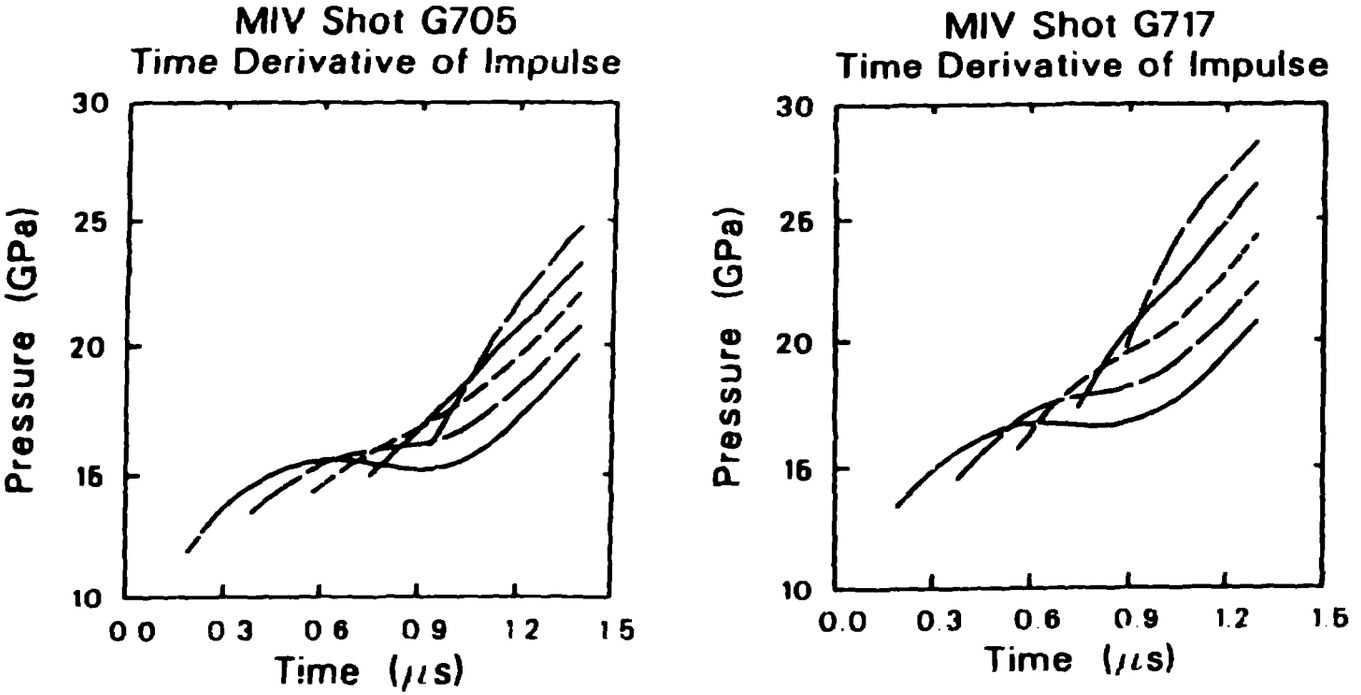

FIGURE 6. PRESSURE AT THE GAUGES (σ_{rr}) FOR SHOTS G705 (LEFT) AND G717 (RIGHT).

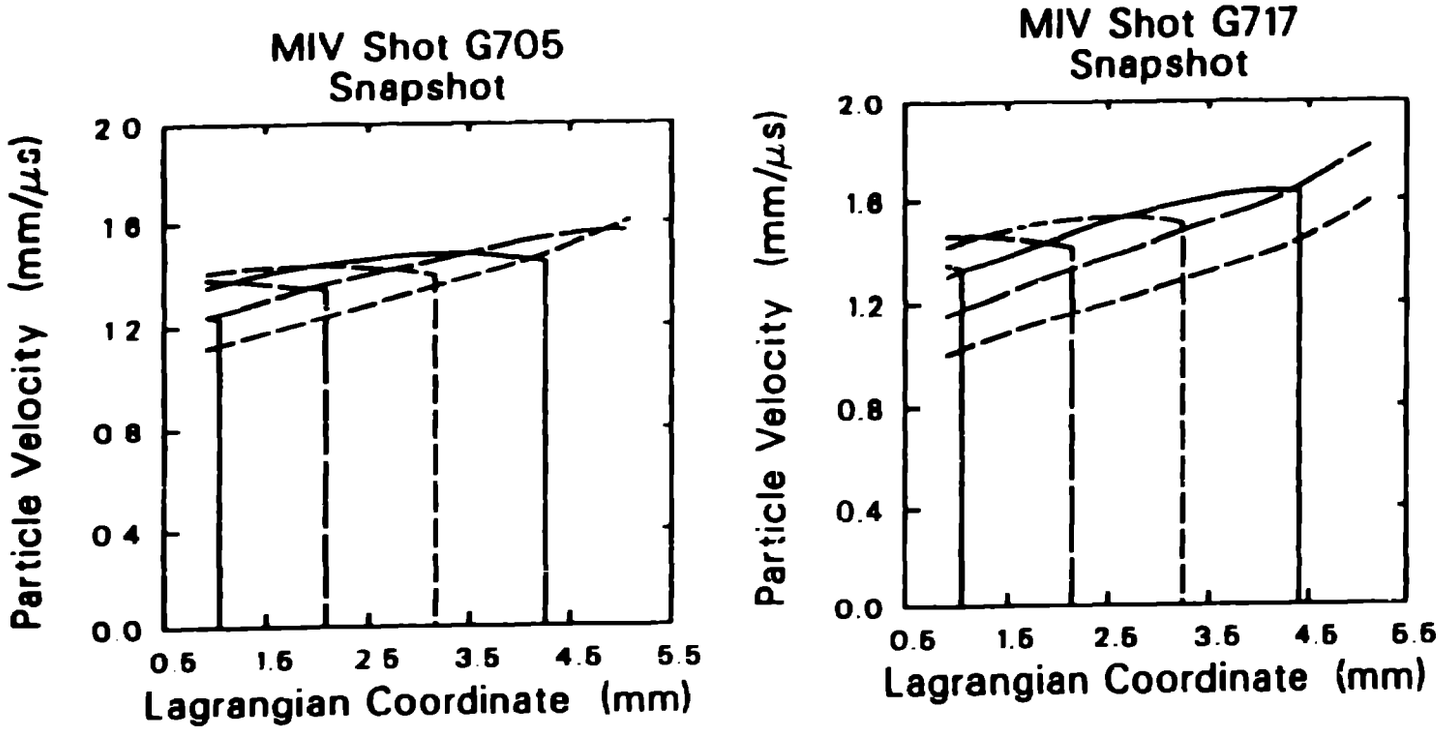

FIGURE 7. PARTICLE VELOCITY SNAPSHOT PRO
FILES AT SIX TIMES ($t = 0.2, 0.4, \cdots, 1.2$) FOR
SHOTS G705 (LEFT) AND G717 (RIGHT).

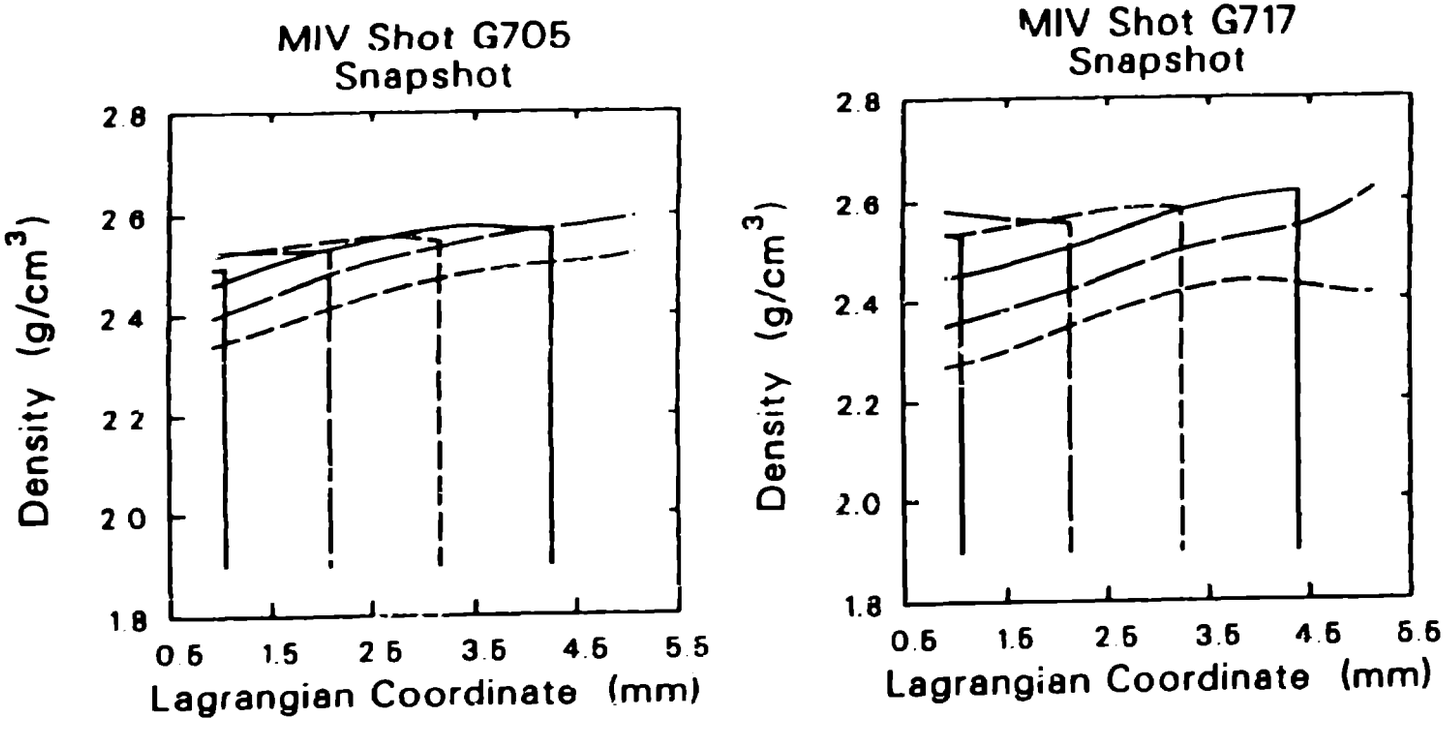

FIGURE 8. DENSITY SNAPSHOT PROFILES AT SIX TIMES ($t = 0.2, 0.4, \cdots, 1.2$) FOR SHOTS G705 (LEFT) AND G717 (RIGHT).

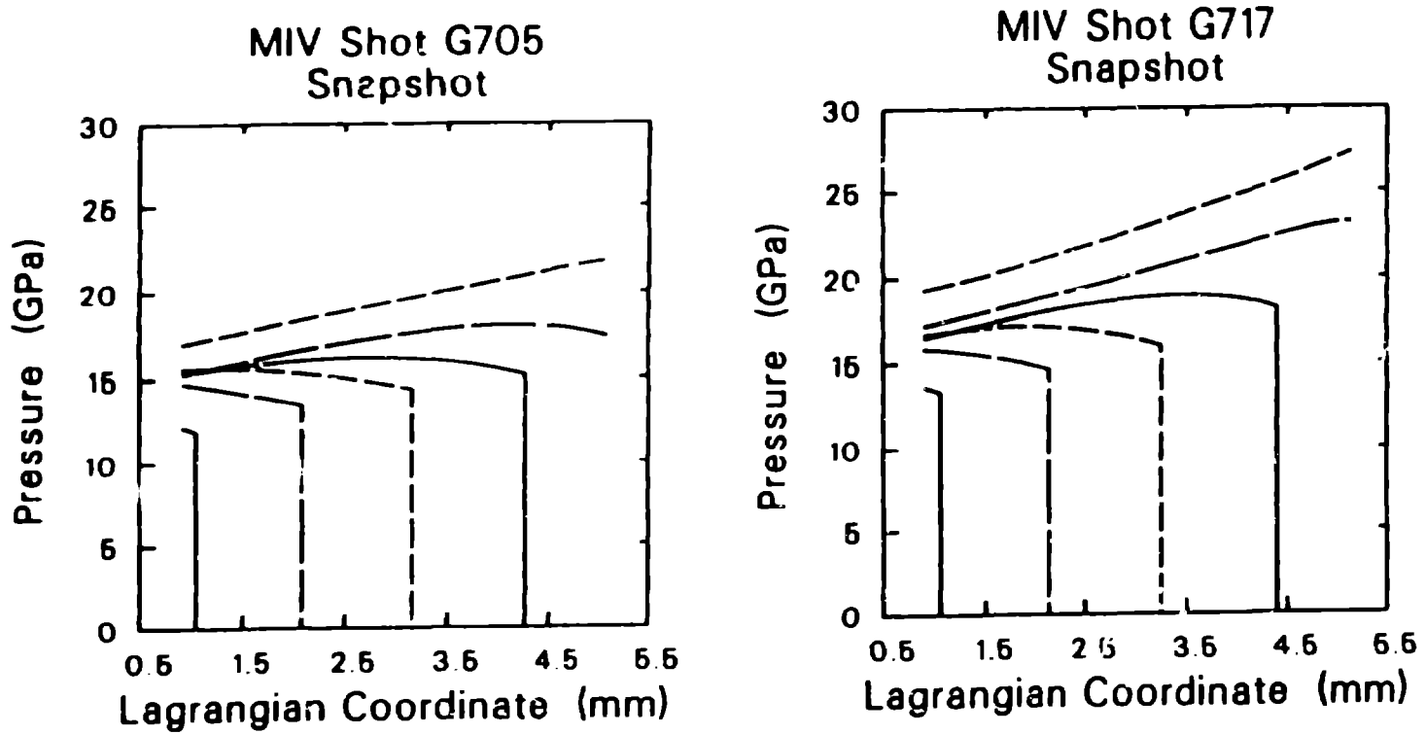

FIGURE 9. PRESSURE SNAPSHOT PROFILES A SIX TIMES ($t = 0.2, 0.4, \cdots, 1.2$) FOR SHOTS 705 (LEFT) AND G717 (RIGHT).

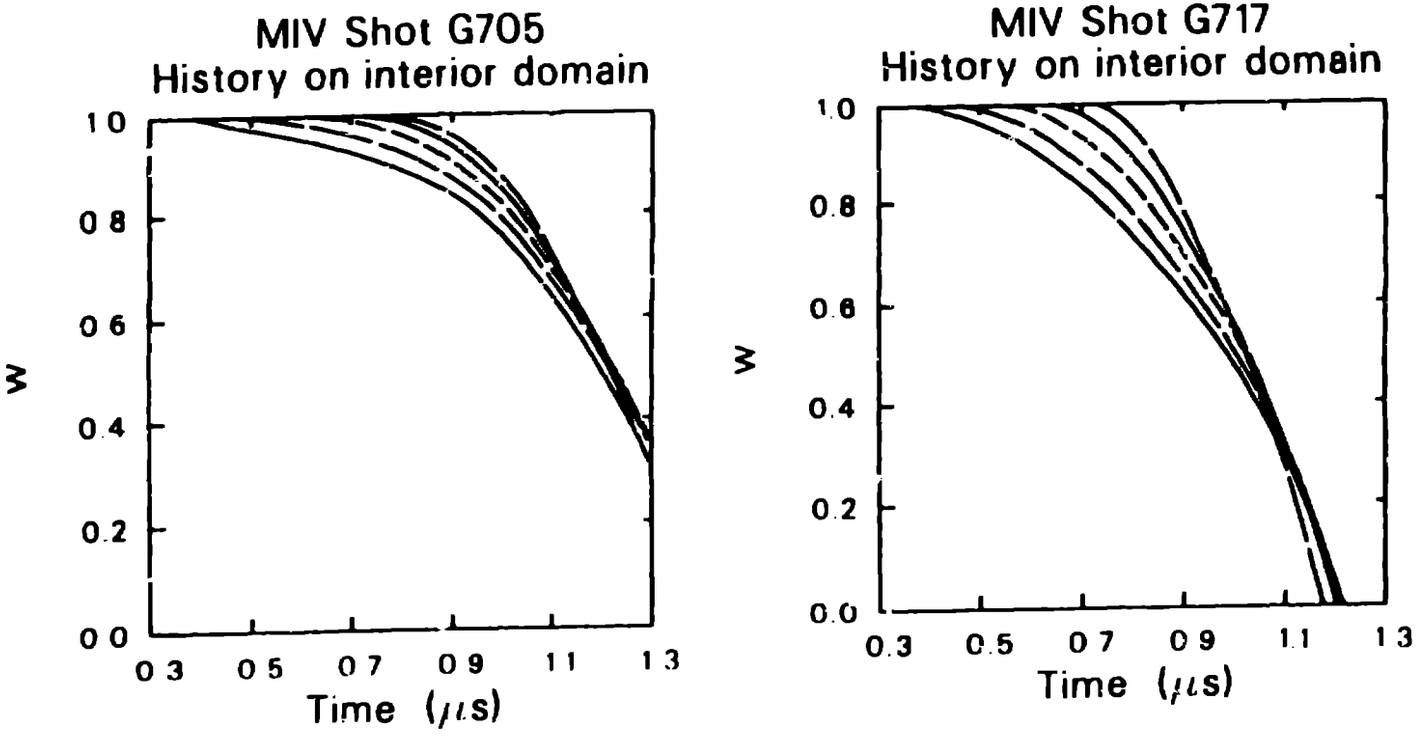

FIGURE 10. MASS FRACTION OF REACTANT HISTORIES AT h = 2.0, 2.5, 3.0, 3.5, and 4.0 FOR SHOTS G705 (LEFT) AND G717 (RIGHT).

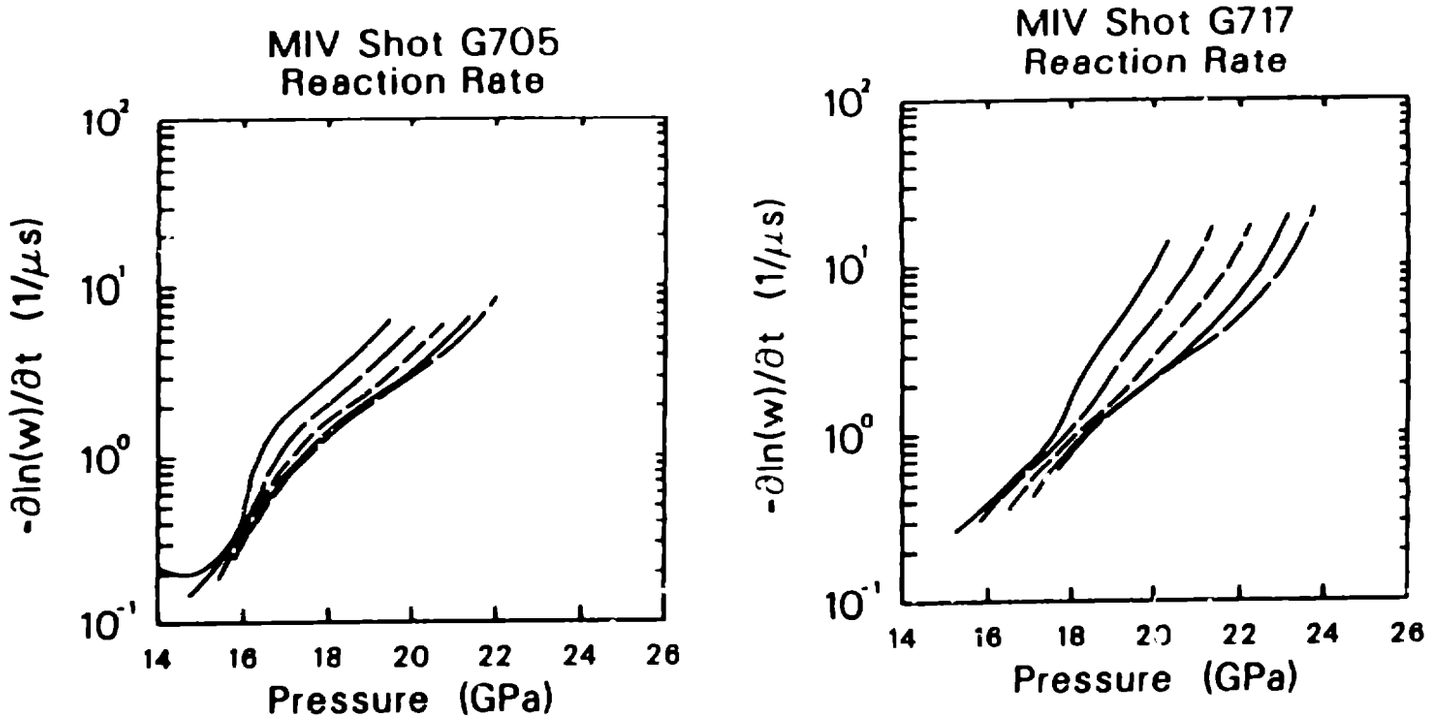

FIGURE 11. TIME DERIVATIVE OF $-ln(w)$ HISTORIES AT h= 2.0, 2.5, 3.0, 3.5 and 4.0 FOR SHOTS G705 (LEFT) AND G717 (RIGHT).

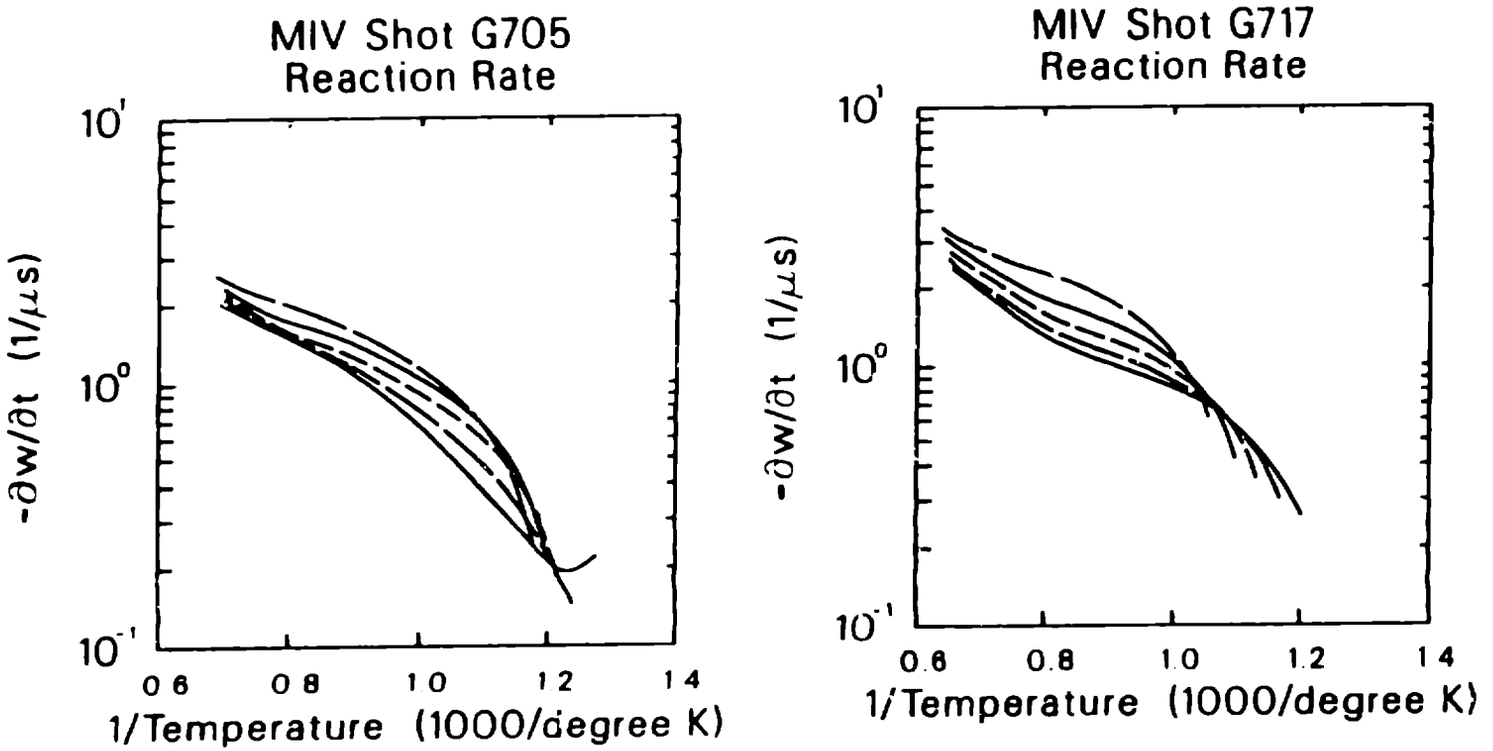

FIGURE 12. REACTION RATE HISTORIES VERSUS EQUILIBRIUM TEMPERATURE AT h= 2.0 2.5, 3.0, 3.5 and 4.0 FOR SHOTS G705 (LEFT) AND G717 (RIGHT).

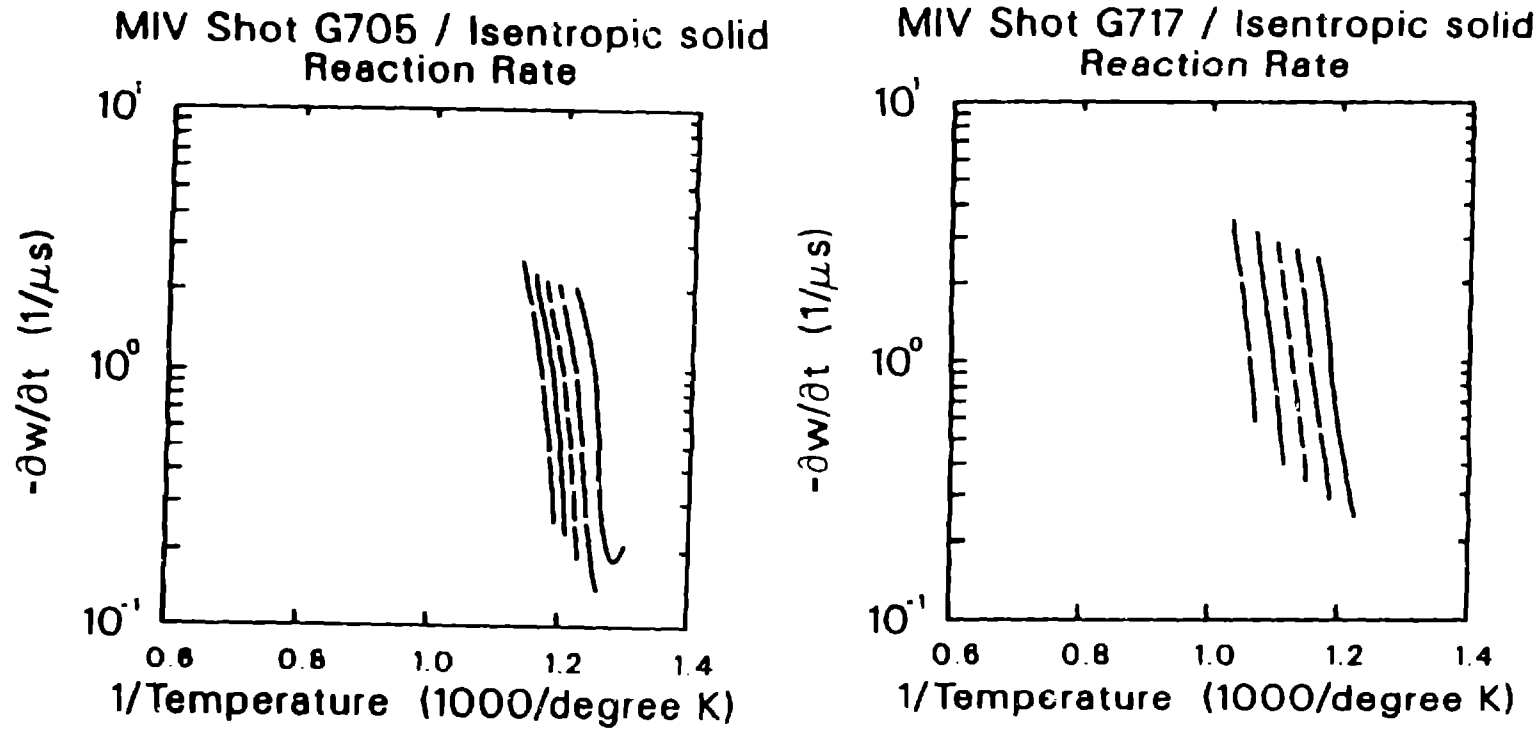

FIGURE 13. REACTION RATE HISTORIES VERSUS ISENTROPIC SOLID TEMPERATURE AT h_i = 2.0, 2.5, 3.0, 3.5 and 4.0 FOR SHOTS G705 (LEFT) AND G717 (RIGHT).